

# A Multifaceted Ferrocene Interlayer for Highly Stable and Efficient Lithium Doped Spiro-OMeTAD-based Perovskite Solar Cells

Thomas Webb,\* Xueping Liu, Robert J.E. Westbrook, Stefanie Kern, Muhammad T. Sajjad, Sandra Jenatsch, K. D. G. Imalka Jayawardena, W. Hashini K. Perera, Igor P. Marko, Sanjayan Sathasivam, Bowei Li, Mozhgan Yavari, David J. Scurr, Morgan R. Alexander, Thomas J. Macdonald, Saif A. Haque,\* Stephen J. Sweeney,\* and Wei Zhang\*

Over the last decade, 2,2'',7,7''-Tetrakis[*N,N*-di(4-methoxyphenyl)amino]-9,9'-spirobifluorene (spiro-OMeTAD) has remained the hole transporting layer (HTL) of choice for producing high efficiency perovskite solar cells (PSCs). However, PSCs incorporating spiro-OMeTAD suffer significantly from dopant induced instability and non-ideal band alignments. Herein, a new approach is presented for tackling these issues using the functionality of organometallobenes to bind to Li<sup>+</sup> dopant ions, rendering them immobile and reducing their impact on the degradation of PSCs. Consequently, significant improvements are observed in device stability under elevated temperature and humidity, conditions in which ion migration occurs most readily. Remarkably, PSCs prepared with ferrocene retain 70% of the initial power conversion efficiency (PCE) after a period of 1250 h as compared to only 8% in the control. Synergistically, it is also identified that ferrocene improves the hole extraction yield at the HTL interface and reduces interfacial recombination enabling PCEs to reach 23.45%. This work offers a pathway for producing highly efficient spiro-OMeTAD devices with conventional dopants via addressing the key challenge of dopant induced instability in leading PSCs.

## 1. Introduction

In recent years, metal halide perovskites have drawn increasing research attention as a promising light-harvesting layer for photovoltaic devices. To date, the use of spiro-OMeTAD as a hole transporting layer (HTL) has been a pre-requisite for producing PSCs with the highest PCEs reaching beyond 25%.<sup>[1–3]</sup> However, whilst enabling the record PCEs, the use of spiro-OMeTAD contributes significantly to the rapid degradation of the perovskite layer. The additional instability imparted on the PSCs from the use of spiro-OMeTAD originates from the dopants added to spiro-OMeTAD which are required to improve the low intrinsic conductivity of the HTL.<sup>[4–6]</sup> As of writing, the highest performing PSCs are prepared using lithium bis(trifluoromethanesulfonyl)imide (LiTFSI) doped spiro-OMeTAD, enabling

T. Webb, X. Liu, K. D. G. I. Jayawardena, W. H. K. Perera, B. Li, M. Yavari, W. Zhang  
Advanced Technology Institute  
Department of Electrical and Electronic Engineering  
University of Surrey  
Guildford, Surrey GU2 7XH, UK  
E-mail: thomas.webb@surrey.ac.uk; wz0003@surrey.ac.uk  
T. Webb, R. J. E. Westbrook, T. J. Macdonald, S. A. Haque  
Department of Chemistry and Centre for Processable Electronics  
Imperial College London  
London W12 0BZ, UK  
E-mail: s.a.haque@imperial.ac.uk

 The ORCID identification number(s) for the author(s) of this article can be found under <https://doi.org/10.1002/aenm.202200666>.

© 2022 The Authors. Advanced Energy Materials published by Wiley-VCH GmbH. This is an open access article under the terms of the Creative Commons Attribution License, which permits use, distribution and reproduction in any medium, provided the original work is properly cited.

X. Liu  
State Centre for International Cooperation on Designer  
Low-Carbon & Environmental Materials (CDLCEM)  
School of Materials Science and Engineering  
Zhangzhou University  
Henan 450001, China  
S. Kern, D. J. Scurr, M. R. Alexander  
School of Pharmacy  
University of Nottingham  
Nottingham NG7 2RD, UK  
M. T. Sajjad  
London Centre for Energy Engineering  
School of Engineering  
London South Bank University  
London SE1 0AA, UK  
S. Jenatsch  
Fluxim AG  
Winterthur 8400, Switzerland

DOI: 10.1002/aenm.202200666

hole mobilities within the HTL of up to  $1.6 \times 10^{-3} \text{ cm}^2 \text{ V}^{-1} \text{ s}^{-1}$ .<sup>[4]</sup> However, the use of such highly hygroscopic lithium salts has been shown to dramatically accelerate the degradation of PSCs.<sup>[5–8]</sup> Previous works have identified that upon doping with LiTFSI, lithium ions can readily become mobile and diffuse within the perovskite layer, forming hygroscopic LiX salts (where X<sup>-</sup> is a halide) which in turn rapidly degrade the perovskite.<sup>[5,9–14]</sup> Wang et al demonstrated that following evaporation of *tert*-butylpyridine (tBP), a common spiro-OMeTAD additive, LiTFSI begins to form hygroscopic aggregates which hydrate the perovskite/spiro-OMeTAD interface degrading the perovskite over a period of < 1000 hours.<sup>[8]</sup> Furthermore, it has also been shown that tBP is, by itself, insufficient to prevent the migration of lithium ions.<sup>[7]</sup> To this extent, Kim et al. recently revealed that the migration of Li<sup>+</sup> is critical in the degradation of spiro-OMeTAD-based devices and is accelerated at higher temperatures, leading to the rapid degradation of the perovskite.<sup>[7]</sup> For these combined reasons spiro-OMeTAD-based PSCs consistently fall short of the practical requirements for the commercialization of solar cells. Indeed, the poor stability of LiTFSI doped spiro-OMeTAD as an HTL has become such a problem that many leading studies using the architecture replace the HTL with a more stable, yet lower efficiency, alternative or omit reporting stability entirely.<sup>[6,15]</sup> Consequently, addressing the impact of lithium on device stability is one of the biggest challenges facing the highest efficiency PSCs.

As of writing, two principal strategies have emerged within the literature for improving the stability of n-i-p PSCs, namely (i) searching for new less destructive dopants or (ii) replacing spiro-OMeTAD in favor of alternative stable HTLs such as poly(triarylamine) (PTAA), poly(3-hexathiophene) (P3HT) or a range of novel molecular transporting materials (Table S1, Supporting Information).<sup>[5,16–18]</sup> While these candidates can yield improvements in the long-term stability, the PCEs of resultant devices remain inferior to the spiro-OMeTAD counterparts. This performance gap has led to a trade-off between efficiency and stability in PSCs. More recently the formation of a blocking layer between the lithium doped spiro-OMeTAD HTL and the perovskite has been suggested using either graphene or flower-like MoS<sub>2</sub>.<sup>[11,19]</sup> Similar to the previous approaches, devices prepared using a blocking layer have yet to match the high efficiencies achieved using the conventional spiro-OMeTAD architecture, reaching up to 20.18% in devices prepared with MoS<sub>2</sub>. Furthermore, by blocking the Li<sup>+</sup> at the interface, the mechanism by which hygroscopic aggregates are formed is not avoided. This challenge, therefore, requires new strategies that target the Li<sup>+</sup> ions within the HTL itself, preventing the accumulation of Li<sup>+</sup> at the interface and subsequent degradation. Very recently, several studies have sought to replace the Li<sup>+</sup> metal cation (M<sup>+</sup>)

in M<sup>+</sup>TFSI<sup>-</sup> in favor of other metal cations including zinc, calcium, magnesium and copper.<sup>[20–22]</sup> Indeed, Seo et al. demonstrated that replacing the Li<sup>+</sup> in favor of Zn<sup>+</sup> improves the stability of the spiro-OMeTAD when illuminated over a period of 600 h.<sup>[21]</sup> Similarly, copper salts including cuprous thiocyanate, cuprous iodide, FK102 and FK209 amongst other copper (II) salts, have been frequently used on their own or as a co-dopant additive with LiTFSI to oxidize spiro-OMeTAD.<sup>[6,23,24]</sup> Recently, Zhu et al. identified that by using FK209, arguably the most common copper-based additive, as a sole p-type dopant, the stability of spiro-OMeTAD could be improved via enhancing the morphology and hydrophobicity. This observation has been frequently reported in copper-based spiro-OMeTAD dopants.<sup>[6,23,24]</sup> However, for optimal hole conduction and subsequent device performance, LiTFSI is required as a co-dopant. In this context, developing strategies that can be easily integrated to improve the long-term stability of the LiTFSI-doped spiro-OMeTAD devices whilst also maintaining high PCEs is essential and a practical choice. Indeed, the use of LiTFSI remains a necessary choice within groups producing the highest efficiency devices. It is therefore essential that efforts are made to address this key challenge at the leading edge of PSC development.

In addition to poor stability, PSCs prepared with spiro-OMeTAD also suffer losses at the perovskite/HTL from the formation of potential barriers with the perovskite, impeding hole extraction and contributing to efficiencies falling short of the Shockley-Queisser (SQ) limit. These barriers lead to losses at the interface, reducing carrier extraction around the open-circuit voltage ( $V_{OC}$ ).<sup>[16–18,25,26]</sup> This has been most frequently reported in formamidinium-based perovskites, essential for high-efficiency PSCs.<sup>[6,27,28]</sup> The poor energy level alignment at the interface leads to the accumulation of carriers at the interface, reducing both the fill factor (FF) and short circuit current density ( $J_{SC}$ ) and contributing to hysteresis phenomena.<sup>[6,25,29,30]</sup> To improve the photovoltaic performance of the spiro-OMeTAD based devices, it is essential to reduce the recombination losses at the interface via means of promoting efficient carrier extraction, reducing carrier accumulation at the interface and effective passivation of trap states.<sup>[31–34]</sup>

Recently, the use of lower-dimensional secondary perovskite phases has gained significant attention as a promising strategy for promoting self-driven carrier separation at perovskite interfaces, enabling efficient hole extraction and improved FFs.<sup>[29,35,36]</sup> However, the approach is highly system dependent and requires careful control of the dimensionality of the lower-dimensional phases.<sup>[36–39]</sup> Recent studies have shown that only  $n = 1$  pure 2D lower dimensional phases are suitable for improving the charge transfer yield at the interface. Westbrook et al. demonstrated that for lower dimensional phases  $n > 1$  charge transport is hindered. The tendency of which lower-dimensional 2D phases are formed is highly sensitive to factors such as composition, annealing time and concentration.

Ferrocene, a sandwich structured organometalocene, is a highly stable and low-cost transition metal complex that undergoes fast electron exchange to form positively charged ferrocenium ions.<sup>[40]</sup> As a consequence, ferrocene has previously been incorporated into dye-sensitized solar cells (DSSCs) as a redox mediator, before being identified as an effective co-mediator when combined with inorganic redox shuttles enabling fast

I. P. Marko, S. J. Sweeney  
Advanced Technology Institute  
Department of Physics  
University of Surrey  
Guildford, Surrey GU2 7XH, UK  
E-mail: s.sweeney@surrey.ac.uk  
S. Sathasivam  
Department of Chemistry  
University College London  
London WC1H 0AJ, UK

regeneration of oxidized sensitizers.<sup>[41–45]</sup> In addition to DSSC technologies, ferrocene has also been used to functionalize a range of organic and inorganic semiconducting materials to improve their electron transfer properties and conductivity.<sup>[46–49]</sup> When applied in organic photovoltaics (OPV) the addition of ferrocene has also been shown to improve carrier mobility and suppress recombination via the volatility of ferrocene and the ability to bridge between organic molecules, ordering the structure.<sup>[50]</sup> More recently, the ferrocenium salt  $\text{Fc}^+\text{PF}_6^-$  has been proposed as an indicator of electron transfer in  $\text{CsPbBr}_3$  nanocrystals for photocatalytic applications, due to its rapid electron transfer kinetics.<sup>[51]</sup>

In this work, we demonstrate how both the key issue of stability and obtaining high charge transfer yields can be addressed simultaneously through developing a ferrocene co-mediator interlayer at the perovskite/spiro-OMeTAD interface. In a key result, we demonstrate this new approach can effectively tackle the challenge of lithium instigated degradation of doped spiro-OMeTAD PSCs. Probing deeper into the mechanism behind this observation, we identify that when incorporated within the spiro-OMeTAD layer, the cyclopentadiene rings of ferrocene can form an adduct with the  $\text{Li}^+$  ions within the HTL preventing  $\text{Li}^+$  migration into the perovskite and aggregation at the interface. Consequently, the  $\text{Li}^+$  ions form a homogeneous distribution throughout the HTL thereby mitigating any migration. By directly targeting the ability of the  $\text{Li}^+$  to become mobile we demonstrate a new approach to address the stability while also encouraging charge extraction at the interface. Consequently, we demonstrate significant improvements in the long-term stability of modified PSCs under elevated humidity and temperature. Indeed, ferrocene modified PSCs retained a remarkable 70% of the initial PCE over 1250 hours when stored in warm humid conditions (60 °C, RH = 50%), compared to only 8% in the conventional control cell. Synergistically, we also observe interactions occurring between ferrocene and the perovskite at the interface which we find improves carrier separation at the perovskite/HTL interface, leading to fast hole extraction and high charge transfer yields. Interestingly, we also reveal that ferrocene can oxidize spiro-OMeTAD when applied either as an interlayer or directly within the precursor, improving the carrier transport properties of the HTL. Without any conventional perovskite passivation procedure, champion devices with a ferrocene co-mediator interlayer exhibited a PCE of 23.45%, a significant increase over the 21.61% recorded in the control devices. The discussed approach is therefore a useful tool for addressing the poor stability of LiTFSI-based PSCs and allowing the stability of spiro-OMeTAD-based PSCs to match the remarkable performance. This study also further probes the exciting new opportunities afforded by the novel properties of metallocenes in semiconductor photovoltaics.

## 2. Results and Discussion

### 2.1. Characterization of Ferrocene Incorporation on $\text{Li}^+$ Ion Migration and the Perovskite Surface

To fabricate the ferrocene modified perovskite/spiro-OMeTAD film, ferrocene (Figure 1a) was dissolved in chlorobenzene

and spin-coated onto a  $(\text{FAPbI}_3)_{0.95}(\text{MAPbBr}_3)_{0.05}$  perovskite thin film. Samples fabricated without the deposition of a ferrocene co-mediator interlayer are hereafter referred to as control samples. A Li-TFSI spiro-OMeTAD layer was next deposited (see experimental section for further details). The location of the as-deposited ferrocene co-mediator modification in a completed PSC stack is shown in Figure 1b. Owing to the solvent orthogonality between the low-polarity chlorobenzene solvent and perovskite layer, no significant changes in the perovskite film (including crystallographic, morphological or optical band gap) were observed (Figures S1–S3, Supporting information). The presence of ferrocene on the perovskite surface was confirmed using energy dispersive X-ray (EDX) spectroscopy which revealed a uniform distribution of Fe across the perovskite surface (Figure S4, Supporting information).

We next used OrbiSIMS (secondary ion mass spectrometry) in dual beam 3D imaging mode with a time of flight (ToF) analyzer<sup>[52]</sup> to depth profile the distribution of ferrocene/ferrocenium ( $\text{Fe}^+$ ) and lithium ( $\text{Li}^+$ ) ions, sputtering from spiro-OMeTAD (Figure 1c) into the perovskite film shown in Figures 1d,e. The measured samples were aged for 200 h within a nitrogen filled glovebox to provide sufficient time for the potential migration of  $\text{Li}^+$  to occur within the films. As expected, in the samples prepared with ferrocene a signal corresponding to  $\text{Fe}^+$  is distributed entirely above the perovskite. The location of the ferrocene is attributed to the processing solvent orthogonality combined with the significant steric bulk of the organometalocene sandwich structure (Figure S5, Supporting information). While a large fraction of ferrocene was located close to the interface between perovskite and spiro-OMeTAD, we also note that a fraction of the ferrocene becomes distributed within the HTL owing to an affinity with the spiro-OMeTAD processing solvents.

Considering next the distribution of the  $\text{Li}^+$  ions, without ferrocene, diffusion occurs from the doped spiro-OMeTAD HTL into the perovskite layer and increases steadily towards the  $\text{SnO}_2$  ETL, consistent with previous reports of lithium diffusion into the perovskite.<sup>[5,7,9,10]</sup> Additionally, accumulation of  $\text{Li}^+$  at the HTL/perovskite interface can also be observed, confirming that destructive hygroscopic LiTFSI aggregates at the perovskite/spiro-OMeTAD interface following the evaporation of tBP after 200 hours, as previously proposed within the literature.<sup>[8]</sup> In comparison, the sample modified with a ferrocene interlayer exhibits a significantly reduced fraction of the  $\text{Li}^+$  migrating within the perovskite and negligible accumulation at the HTL/perovskite interface. This effect is evident in both the depth profiles (Figures 1d,e) and 3D reconstructed secondary ion imaging (Figures 1f,g). We note that variations in absolute counts of  $\text{Li}^+$  dopant and  $\text{C}_{14}\text{H}_{14}\text{NO}_2^+$  between the samples with and without ferrocene are an artefact of matrix effects. The matrix artefacts do not affect the relative profile moving from the HTL into the perovskite.<sup>[53]</sup> We note identical LiTFSI doped spiro-OMeTAD solutions were used to prepare both the films with and without the incorporation of ferrocene, ensuring identical LiTFSI concentrations in both samples.

To rationalize the reduced  $\text{Li}^+$  migration out of the HTL and into the perovskite the possibility of an adduct formation between ferrocene and Lithium ions was investigated.  $^7\text{Li}$  nuclear magnetic resonance (NMR) spectroscopy was collected from solutions of LiTFSI with and without the addition of

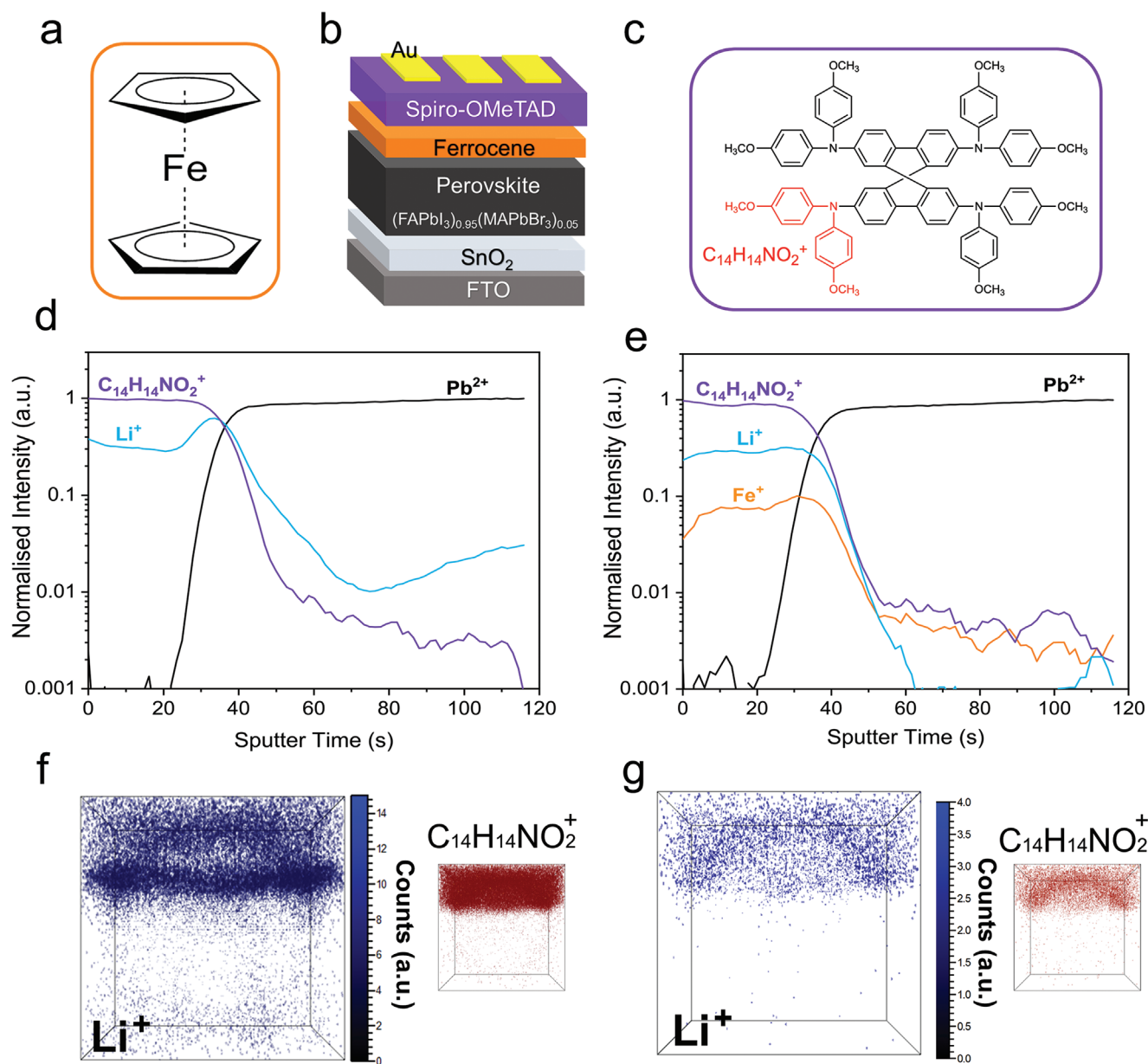


**Figure 1.** a) Structure of ferrocene sandwich complex. b) Device architecture and location of ferrocene in preparing perovskite solar cells. c) Structure of spiro-OMeTAD, (red)  $C_{14}H_{14}NO_2^+$  fragment tracked in SIMS measurements. d) OrbiSIMS depth profiles of control perovskite/spiro-OMeTAD sample after 200 h in  $N_2$ ,  $Pb^{2+}$  signal corresponding to perovskite normalized to  $C_{14}H_{14}NO_2^+$  attributed to the methoxyphenol amine branches of spiro-OMeTAD. e) OrbiSIMS depth profiles of ferrocene treated perovskite/ferrocene/spiro-OMeTAD sample after 200 h in  $N_2$ , additional  $Fe^+$  is attributed to the incorporation of ferrocene. f) 3D reconstructed secondary ion images of  $Li^+$  (left, blue) and  $C_{14}H_{14}NO_2^+$  fragment of spiro-OMeTAD (right, red) in films prepared without ferrocene, g) 3D reconstructed secondary ion images of  $Li^+$  (left, blue) and  $C_{14}H_{14}NO_2^+$  fragment of spiro-OMeTAD (right, red) in films prepared with ferrocene, identical solutions of doped spiro-OMeTAD were used for both OrbiSIMS measurements, variations in the absolute intensity of counts are attributed to matrix effects.

ferrocene as seen in **Figure 2a**. From the collected spectra it is apparent that the addition of ferrocene to LiTFSI leads to a significant shielding of the  $Li^+$  nuclei consistent with the pushing of electron density from the electron-rich cyclopentadiene anions of the metallocene onto the  $Li^+$  nuclei. Similar interactions occurring between ferrocene and group 1 alkali metals have previously been proposed within the literature, suggesting that electron density may be donated from the outward-facing

$\pi$  orbitals of the cyclopentadiene rings. However, experimental evidence of this theory has been limited.<sup>[54,55]</sup> To offer further clarity in this matter,  $^{13}C$  NMR was used to compare the shifts of the cyclopentadiene rings of ferrocene before and after forming an adduct with the  $Li^+$  ions as shown in **Figure 2b**. Consistent with the previous theoretical studies, following the formation of the adduct with  $Li^+$  ions the carbon becomes less shielded, indicating the loss of electron density. The reaction of  $Li^+$  and

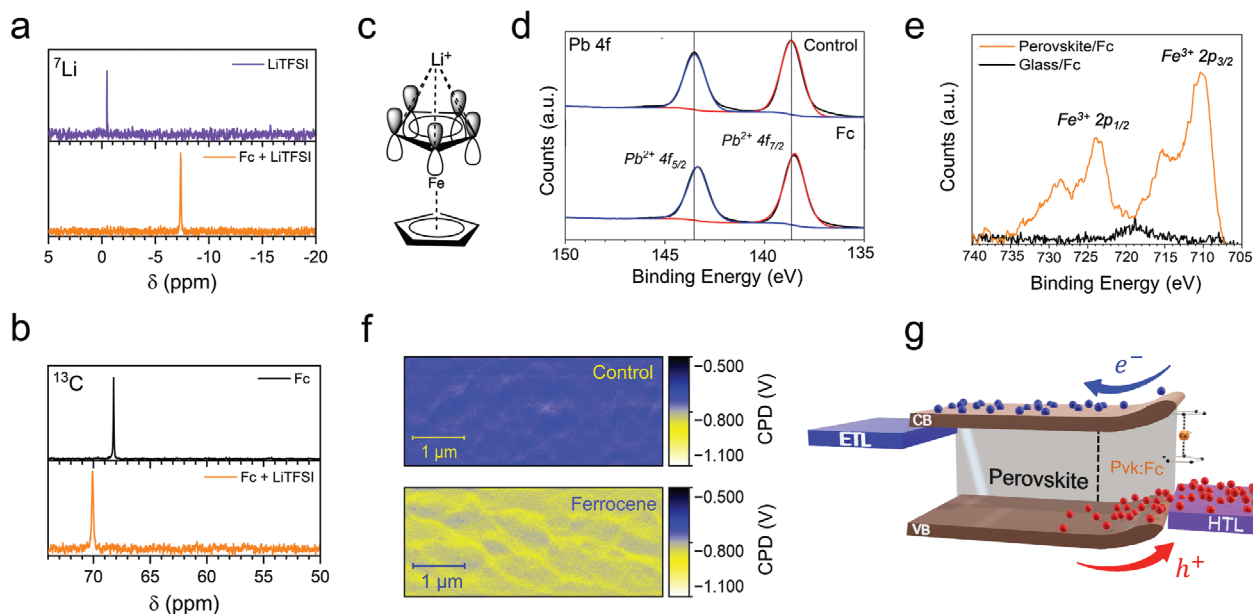


**Figure 2.** a)  $^7\text{Li}$ -NMR of LiTFSI (purple) and LiTFSI upon addition of ferrocene (Fc) (orange), b)  $^{13}\text{C}$ -NMR of ferrocene (black) and ferrocene upon addition of LiTFSI (orange). c) Schematic of electron donation from the cyclopentadiene aromatic ring onto the lithium cations. d) XPS spectra of the shift in Pb 4f orbitals following deposition of ferrocene. e) XPS of Fe 2p orbitals when deposited on perovskite, absence of ferrocene Fe 2p orbitals when deposited on glass is attributed to sublimation of ferrocene within the XPS vacuum. f) KPFM surface potential scans of control perovskite surface (top) and after deposition of ferrocene (bottom). g) Representation of proposed carrier behavior in the ferrocene modified perovskite/HTL interface leading to reduced electron density at the HTL interface.

ferrocene also results in a minor color change in the ferrocene as compared to a reference solution, attributed to the removal of electron density from the conjugated  $\pi$  system depicted in Figure 2c. As a result of the formation of a ferrocene- $\text{Li}^+$  adduct, the mobile  $\text{Li}^+$  ions within the HTL become immobilized, as demonstrated by the previously discussed OrbiSIMS measurements (Figure 1d,e). As such, ferrocene presents a promising approach for tackling the challenge of dopant migration, promoting a homogenous of dopant throughout the HTL.

In addition to forming an immobile adduct with lithium within the HTL, OrbiSIMS and EDX measurements also indicate an accumulation of iron-based species on the surface of the perovskite. Interestingly, X-ray photoelectron spectroscopy of the perovskite films prepared with ferrocene reveals a minor shift in the binding energy (BE) of the lead 4f orbitals to lower binding energies consistent with increased electron density as shown in Figure 2d. Accordingly, spectra collected of the Fe 2p orbital show that the iron exists in a  $\text{Fe}^{3+}$  state with a BE energy of 710 eV, higher than the 707 eV previously reported for  $\text{Fe}^{2+}$  (Figure 2e).<sup>[56–58]</sup> The oxidation of ferrocene upon deposition of the lead perovskite is an interesting result and is consistent with the minor increase in the electron density on the Pb 4f orbitals. While the nature of these reactions is beyond the scope of this study, we note the recent work by Chang et al. who proposed that interactions can occur between Ferrocene and iodine defects yielding  $\text{FcPbI}_3$  and  $\text{Fc}^+\text{I}^-/\text{Fc}^+\text{I}_3$ .<sup>[59]</sup> This is supported by a minor decrease in binding energy in the I 3d XPS spectra, possibly occurring from the  $\text{I}^-$  formation (Figure S6, Supporting Information). Interestingly when collecting reference spectra ferrocene in either the powder form or deposited on glass, the ferrocene

sublimed under the vacuum leading to no signal in the XPS. Indeed, Fe signals could only be achieved when measuring on a perovskite surface, attributed to the formation of interactions with the surface. It is therefore unsurprising that a small passivating fraction of the ferrocene remains adhered to the perovskite surface during the deposition of the spiro-OMeTAD film, while a large fraction becomes redistributed within the HTL.

To further understand the effect of the interaction between the perovskite and the perovskite surface, kelvin probe force microscopy (KPFM) was used to characterize the change in potential of the perovskite at the interface. The KPFM was conducted in the dark with and without the deposition of ferrocene. While XPS reveals the existence of ferrocene on the perovskite film, the thickness of the film could not be accurately measured using standard profilometry techniques, suggesting a thickness of the ferrocene layer of under 10 nm, meaning insulating effects should not occur. Comparing the surface scans of the films prepared with and without ferrocene, a more negative surface potential is recorded in films with ferrocene decreasing from a contact potential difference (CPD) of  $-0.733$  V in the control to  $-0.845$  V upon addition of ferrocene shown in Figure 2f.<sup>[60]</sup> The shift in CPD corresponds to a deeper work function perovskite following the addition of ferrocene. In good agreement with the EDX, the KPFM shows excellent uniformity of the potential across the surface, further suggesting excellent coverage. From the XPS and KPFM, we propose that the deposition of ferrocene on the surface of the perovskite could lead to band bending as depicted in Figure 2g. Similar band bending following treatment of the perovskite surface has previously been reported within the literature.<sup>[61]</sup>

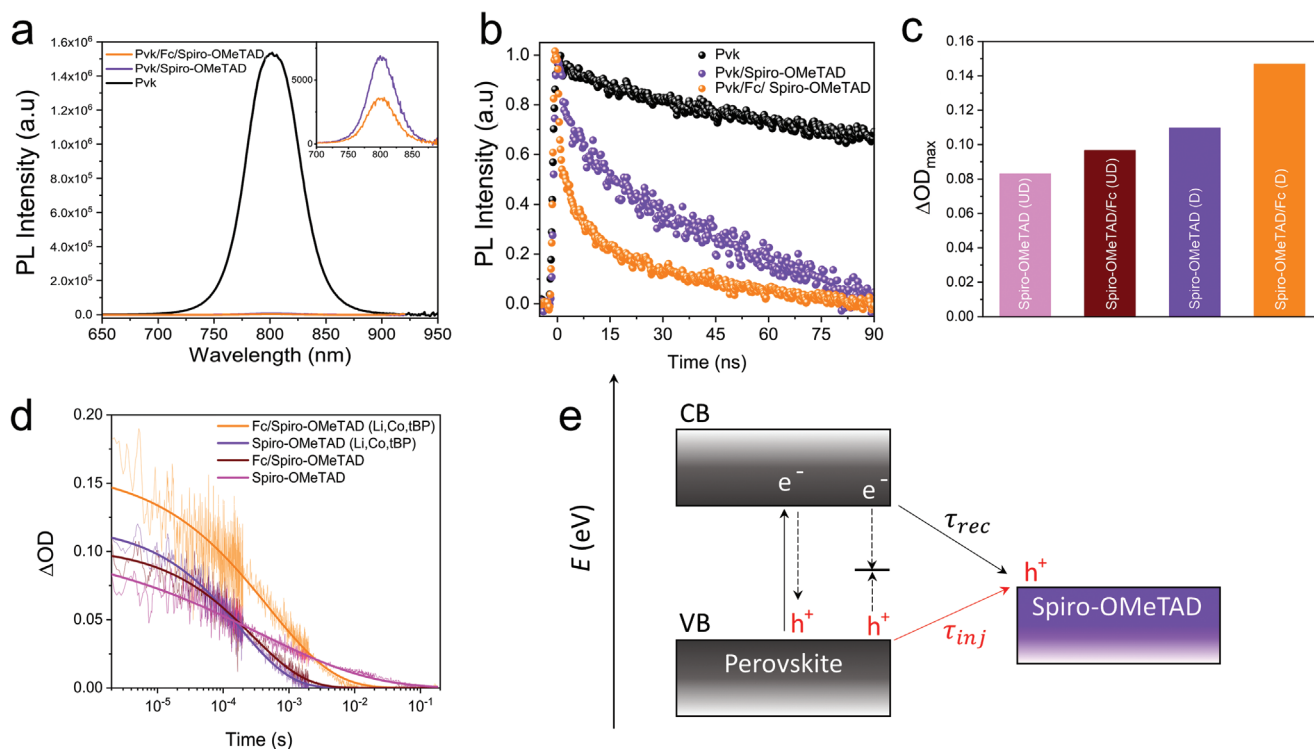


**Figure 3.** a) Steady-state photoluminescence and, b) TRPL decay of films with and without ferrocene layer. c) Comparison of maximum intensity of the [spiro-OMeTAD]<sup>+</sup> transient optical feature with LiTFSI, FK209 and tBP as dopants (D) and without LiTFSI, FK209 and tBP referred to as “undoped” (UD). d) TAS spectra of the NIR spectral region corresponding to the decay of hole polarons (spiro-OMeTAD<sup>+</sup>) of spiro-OMeTAD following excitation of perovskite at 510 nm. e) Schematic of carrier behavior at the perovskite/HTL interface following excitation, where  $\tau_{inj}$  and  $\tau_{rec}$  are the lifetimes of hole injection into the spiro-OMeTAD and bimolecular recombination between the perovskite conduction band and spiro-OMeTAD, respectively.

## 2.2. Charge Carrier Dynamics at the Perovskite/Spiro-OMeTAD Interface

Next, we consider the effect of the ferrocene on the perovskite surface on the charge carrier dynamics at the interface between the perovskite and spiro-OMeTAD. From steady-state photoluminescence (PL) spectroscopy, we observe significant PL quenching in perovskite films prepared with a spiro-OMeTAD layer as compared to those without, attributed to the extraction of photoexcited holes in the former as seen in **Figure 3a**. Upon addition of a ferrocene interlayer between the perovskite and spiro-OMeTAD, we observe a further decrease in PL intensity of 41%, compared to the perovskite/spiro-OMeTAD films without ferrocene interlayer (Figure S7, Supporting Information). In the absence of changes to the perovskite roughness and optical absorption, the observed decrease in PL intensity between the perovskite/spiro-OMeTAD samples with and without ferrocene is attributed to improved extraction of carriers across the interface.

To further investigate the change in hole extraction across the interface, time-resolved photoluminescence (TRPL) measurements were conducted. The TRPL measurements reveal improvements to the charge extraction in the ferrocene modified samples as seen in **Figure 3b**, further consolidating the steady-state PL result. Fitting the TRPL decay with a weighted bi-exponential decay model we observe significantly reduced lifetimes for both fast and slow components, from  $2.0 \pm 0.2$  ns

(3%) and  $41 \pm 4$  ns (97%) in the spiro-OMeTAD reference to  $1.0 \pm 0.1$  ns (8%) and  $30 \pm 3$  ns (92%) in the films with ferrocene interlayers. To extract the charge extraction efficiency ( $\phi$ ) from the TRPL decay, the fraction of quenched to unquenched charges was estimated using the integrated area under the TRPL decays (Table S1 and Note S1, Supporting Information). Indeed, the faster carrier extraction leads to a significant increase in  $\phi$  from  $61 \pm 3\%$  to  $78 \pm 4\%$ . Interestingly, we find that the charge extraction efficiency increases with the increasing concentration of ferrocene modification (Figure S8, Supporting Information). This trend further demonstrates the benefits of ferrocene between the perovskite and HTL, to promote efficient carrier transfer.

To further corroborate the TRPL findings, transient absorption spectroscopy (TAS) measurements were carried out on ferrocene modified perovskite/spiro-OMeTAD films. This technique allows tracking of the development, transfer, and relaxation of excited states, provided those processes involve a change in the absorption characteristics of the film (change in optical density  $\Delta OD$ ). In this experiment, the hole polaron of spiro-OMeTAD at 1600 nm was tracked following excitation of the perovskite at 510 nm.<sup>[62–67]</sup> Exciting at this wavelength ensures that the photogenerated charges are formed within the perovskite layer alone, and therefore any polaronic absorption at 1600 nm can be attributed to injected holes from the perovskite to the spiro-OMeTAD layer.<sup>[64–67]</sup> Given this assignment, we define the relative hole injection yield,  $\Delta OD_{max}$  as the  $\Delta OD$

at  $t = 1 \mu\text{s}$ .<sup>[63]</sup> As such, a significant increase in  $\Delta OD_{max}$  is present in ferrocene modified films as compared to ferrocene-free controls as shown in Figure 3c. This observation is consistent with a higher yield of hole transfer as per the Beer-Lambert law.<sup>[63]</sup> Moreover, the approximately 34% increase in the initial  $\Delta OD$  signal is consistent with the PL data (Figures 3a,b) and indicates that the higher magnitude of PL quenching observed in ferrocene modified films is directly correlated to an increase in the hole extraction yield.<sup>[38]</sup> To further investigate the effect of ferrocene on hole transfer, additional films were prepared without typical dopants (LiTFSI, FK209 or tBP). These films also showed significant improvements in  $\Delta OD_{max}$  compared to the undoped reference spiro-OMeTAD, offering an interesting new strategy for dopant-free spiro-OMeTAD-based PSCs.

We further estimate the charge recombination lifetime of the spiro-OMeTAD hole polaron,  $\tau_{rec}$ , as the time taken for  $\Delta OD_{max}$  to reach 50% of its original value using the full decay of the spiro-OMeTAD transient species (Figure 3d).<sup>[63]</sup> In the absence of an Au electrode on the spiro-OMeTAD, the decay of the injected hole population following excitation has been demonstrated to occur from bimolecular recombination across the interface between accumulated electrons in the perovskite conduction band and free holes in the Spiro-OMeTAD

as depicted in Figure 3e (Note 2 and Figure S9, Supporting Information).<sup>[63,68]</sup> Fitting the hole polaron decay, we observe an increase in  $\tau_{rec}$  from  $0.180 \pm 0.020$  ms in the film prepared with spiro-OMeTAD directly deposited on perovskite compared to  $0.486 \pm 0.004$  ms in the film with a ferrocene interlayer, indicating slower recombination across the interface in the presence of ferrocene. The slower rate of recombination in the ferrocene-containing film is attributed to a reduction in the electron population within the perovskite at the perovskite/spiro-OMeTAD interface as discussed within the literature.<sup>[64–67]</sup> This result is consistent with the ferrocene-induced modification of the surface potential which acts to direct electrons away from the HTL interface, as previously discussed within this work and the literature.<sup>[61]</sup> Combined with the TRPL decays, we demonstrate the addition of ferrocene promotes an increase in the rate of holes injection into the spiro-OMeTAD ( $\tau_{inj}$ ) and a decrease in the rate of back recombination of injected charges ( $\tau_{rec}$ ) (Figure 3e), needed for sustained efficient charge separation and low hysteresis in perovskite solar cells as we will show evidence for in the following section.<sup>[62,63]</sup> The faster hole extraction combined with the reduced rate of recombination at the HTL interface also accounts for the increased  $\Delta OD_{max}$  values obtained in samples prepared with ferrocene.

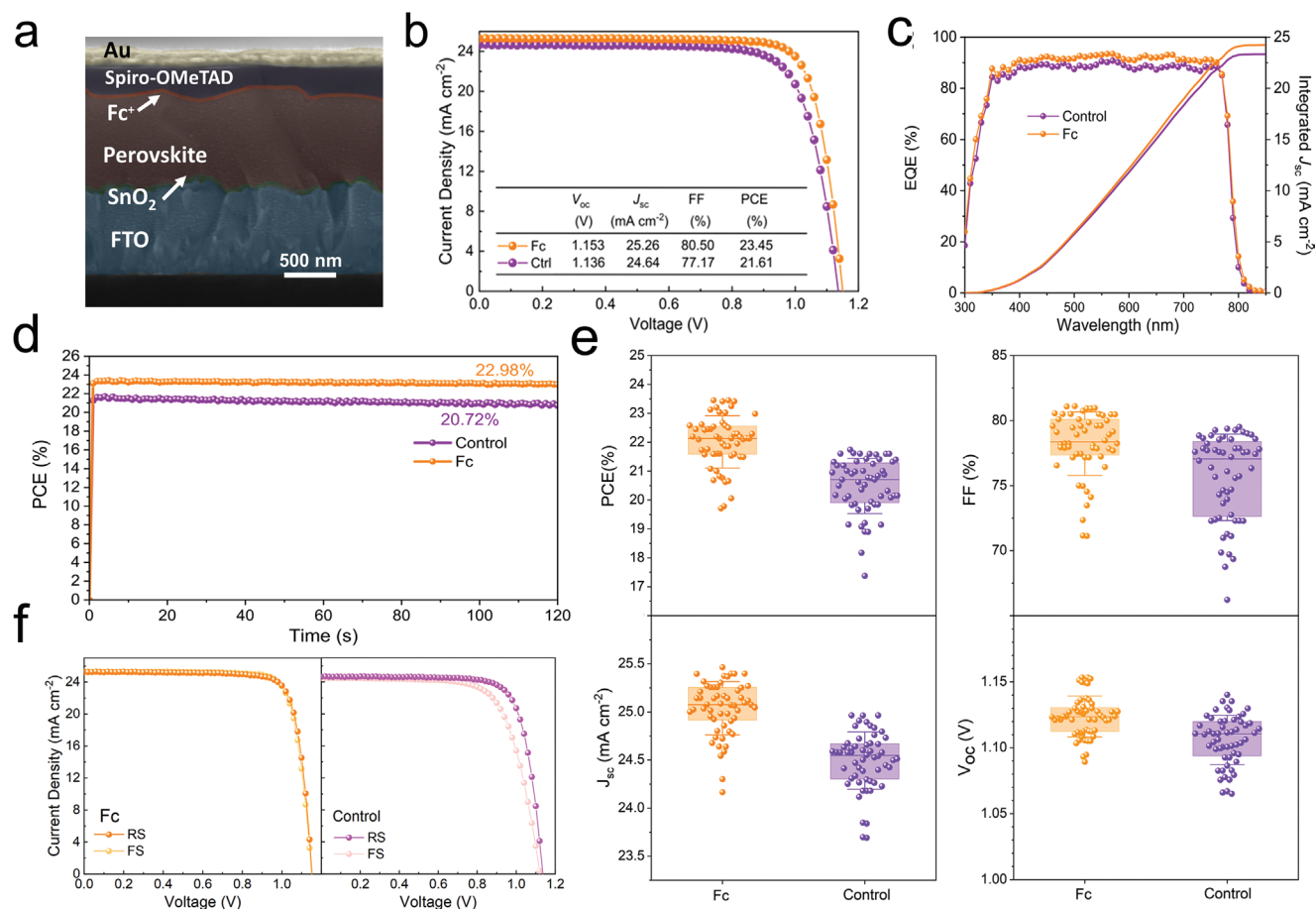


**Figure 4.** a) Cross-section of PSC with ferrocene with structure highlighted. b)  $J$ - $V$  curves of champion PSCs prepared with and without ferrocene. c) EQE and integrated current of PSCs with and without ferrocene. d) MPP tracking of PSCs with and without ferrocene. e) Statistical device data for ferrocene and control devices based on 55 pixels for each. f) Forward (FS) and reverse (RS) scans of PSCs prepared with ferrocene (left) and without ferrocene (right).

### 2.3. Photovoltaic Performance

To demonstrate the effectiveness of the ferrocene interlayer on both device stability and efficiency, PSCs were fabricated using an FTO/SnO<sub>2</sub>/perovskite/ferrocene/spiro-OMeTAD/Au architecture as shown in Figure 4a. In the control device a respectable PCE of 21.61% (statistical mean of 20.45 ± 0.97% for 55 devices) was obtained, with a  $J_{SC}$  of 24.64 mA cm<sup>-2</sup> (24.48 ± 0.29 mA cm<sup>-2</sup>),  $V_{OC}$  of 1.136 V (1.10 ± 0.019 V) and FF of 77.17% (75.57 ± 3.39%). In comparison, PSCs prepared using an optimized concentration of ferrocene (10 mg mL<sup>-1</sup>) (Figure S10, Supporting Information) enabled a champion cell with a significantly improved PCE reaching 23.45% (22.01 ± 0.90%), with a  $J_{SC}$  of 25.26 mA cm<sup>-2</sup> (25.04 ± 0.27 mA cm<sup>-2</sup>),  $V_{OC}$  of 1.153 V (1.12 ± 0.015 V) and FF of 80.50% (78.21 ± 2.43%) as seen in Figure 4b. The improvements in all the photovoltaic parameters of the PSCs prepared with ferrocene are in good agreement with the previously presented discussion of improved carrier extraction and reduced recombination at the interface, as will be later be discussed in further detail.

To ensure accurate calibration of the solar simulator, external quantum efficiency (EQE) measurements were collected. When integrated over the standard AM 1.5 solar emission spectrum, the cells give values of 23.3 and 24.2 mA cm<sup>-2</sup> for the control and ferrocene modified cells respectively, as shown in Figure 4c. The discrepancy between the  $J_{SC}$  collected from EQE and the solar

simulator is calculated as < 5%. The greater EQE of ferrocene-treated PSCs is in line with the evidence that the hole transfer yield is increased in this case. To further confirm the reported PCE, maximum power point (MPP) tracking was conducted on devices prepared with and without ferrocene, yielding sustained PCEs of 22.98% and 20.72% in PSCs fabricated with and without ferrocene, respectively (Figure 4d). For statistical data of the effect of ferrocene on device performance, a set of 55 devices were prepared and measured (Figure 4e). From the statistical data, it is evident that the variability between PSCs is reduced, and reproducibility improved in the devices prepared with the ferrocene interlayers. In addition, the PCE improvement recorded in the champion cells is confirmed with an increase in average efficiency from 20.45 ± 0.97% to 22.01 ± 0.90%. Consistent with the champions cell, the device statistics also confirm enhancements across all photovoltaic parameters. Calculating the hysteresis index (HI) from the forward and reverse scans a significant reduction from 9.5 to 0.2 is observed, between the control and ferrocene modified PSCs respectively shown in Figure 4f. The reduction in hysteresis is attributed in part to the reduced mobility of the ferrocene-bound Li<sup>+</sup> ions, where mobile Li<sup>+</sup> ions have been frequently reported to contribute to hysteresis phenomena in LiTFSI doped spiro-OMeTAD devices.<sup>[5,14,69]</sup>

To further investigate the role of the efficient interfacial hole transfer enabled by ferrocene, and the improvements recorded in the operational PSCs fabricated with ferrocene, transient

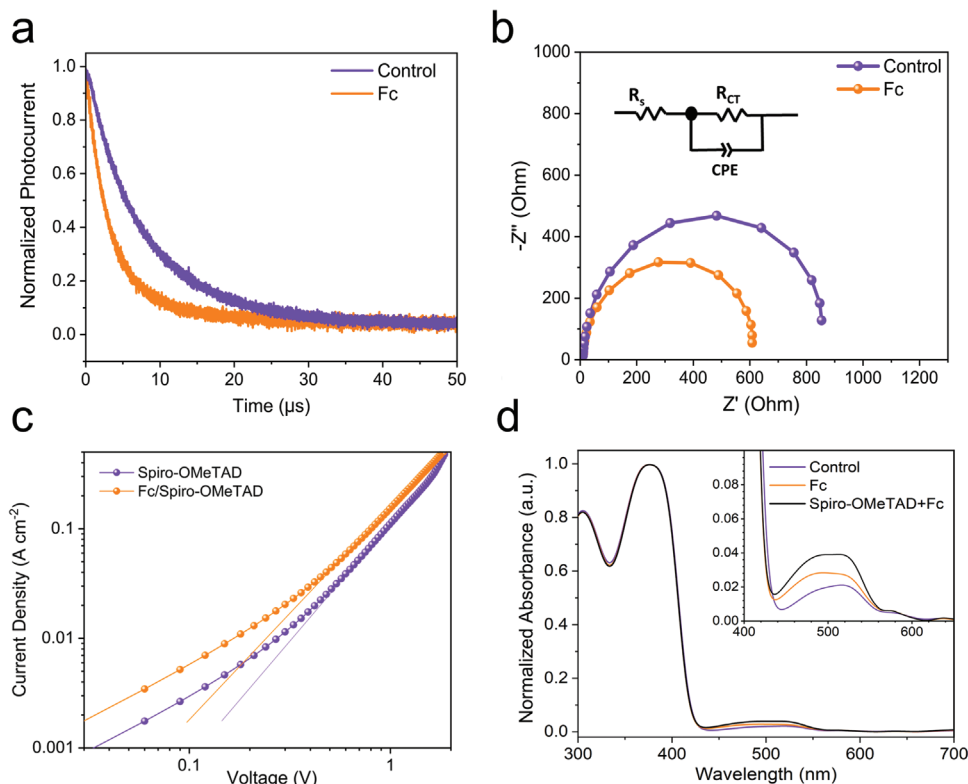


**Figure 5.** a) Normalized TPC decay of PSCs prepared with and without ferrocene held at the open-circuit voltage using a white LED b) Nyquist plot of PSCs electronically biased at 1 V without illumination. c) Log-log current-density voltage plot of hole-only SCLC devices, gradient taken in the fitted region ( $J = V^2$  region) of 1.94 and 1.95 respectively. d) UV-visible absorbance spectra of spiro-OMeTAD prepared without ferrocene (purple), spiro-OMeTAD deposited on a ferrocene layer (orange) and with 10 mg mL<sup>-1</sup> directly added to the spiro-OMeTAD solution (black). Spectra are normalized to the absorbance of the neutral spiro-OMeTAD peak at 385 nm. Inset shows magnification of oxidized spiro-OMeTAD<sup>+</sup> peak at 500 nm.<sup>[72]</sup>

photocurrent (TPC) measurements were conducted and are shown in Figure 5a. Fitting the photocurrent decays with a monoexponential fit reveals a decrease in carrier extraction time of the carriers from  $7.47 \pm 0.41 \mu\text{s}$  in the control device, to  $3.41 \pm 0.18 \mu\text{s}$  in the ferrocene modified device (Figure S11, Supporting Information). Electrochemical impedance spectroscopy (EIS) was measured at a bias close to that of the TPC (1 V) to further study the hole extraction at the perovskite/spiro-OMeTAD interface in PSCs when modified with ferrocene. The collected impedance spectra was fitted with a Randles equivalent circuit containing a constant phase element (CPE). From the Nyquist plots, a decrease in the charge transfer resistance is observed in PSCs modified with the ferrocene. Fitting the Nyquist plots, a reduction of  $R_{CT}$  from  $41.6 \pm 0.4$  to  $29.1 \pm 0.2 \Omega$  is obtained as seen in Figure 5b. The shorter TPC lifetimes in PSCs prepared with ferrocene, combined with decreased  $R_{CT}$  resistance confirms the improved hole extraction efficiency previously identified in the TRPL and TAS spectroscopy occurs within the full PSC under operation. Put together, the characterization of the enhanced hole extraction at the perovskite/spiro-OMeTAD rationalizes the statistical increase in the  $J_{sc}$  and FF in the ferrocene-containing PSCs and is consistent with the previous discussion of an improvement in the energy offset between the spiro-OMeTAD and perovskite valence band.<sup>[25]</sup>

To investigate the photovoltage enhancement in the PSCs whilst also ensuring that the shorter lifetimes observed in the TPC occur from enhanced hole extraction, transient photovoltage (TPV) decays were also collected. In this experiment, as per the TPC, we measured the PSCs under illumination at 1 V near-open circuit conditions, mimicking the conditions used for the TAS experiment. Here, we observe an extended photovoltage decay in devices with the ferrocene interlayers (Figure S12, Supporting Information). Recombination at the interface is therefore reduced within the working PSCs modified with an optimal concentration of ferrocene. The decrease in recombination is in excellent agreement with the longer  $\tau_{rec}$  values recorded in the TAS measurements, which is consistent with a reduced electron population at the perovskite/spiro-OMeTAD interface occurring from a localized driving force directing electrons away from the interface. The reduced electron population at the HTL interface translates to reduced monomolecular recombination of free carriers at the interface producing a more carrier selective interface with longer photovoltage decays in the ferrocene-containing PSCs.<sup>[70]</sup> The reduced recombination at the interface was further probed by measuring the illumination intensity dependence of the photovoltage. The light intensity dependence of the photovoltage of the PSCs reveals a reduction in ideality factor of the slope in the ferrocene-containing PSCs reducing from  $n = 1.55$  to  $1.22$  (Figure S13, Supporting Information). The lower ideality factor in the ferrocene modified devices confirms that the reduced electron population at the HTL interface correlates to reduced Shockley-Read-Hall monomolecular at the interface between perovskite and spiro-OMeTAD. This rationalizes the improvements in  $V_{oc}$  recorded in PSCs prepared with ferrocene.<sup>[71]</sup>

We next consider the implications of the ferrocene diffusion into the spiro-OMeTAD, as observed from the OrbiSIMS (see Figure 1e), on the device performance. Preventing the mobilization of  $\text{Li}^+$  ions within PSCs is essential to improving the stability of spiro-OMeTAD-based PSCs. However, of equal

importance is retaining the remarkable charge-transporting properties of the spiro-OMeTAD layer. To this end, space charge limited current (SCLC) devices were prepared using an ITO/Spiro-OMeTAD/Au configuration, with and without a ferrocene interlayer on the ITO. If charge injection into the spiro-OMeTAD occurs via an ohmic contact, the current density through the device will become limited by the build-up of space-charge within the film with increasing voltage.<sup>[73,4]</sup> Under SCLC conditions ( $J \sim V^2$ ) the carrier mobility is related to the current density as per the Mott-Gurney Law (Equation 1), assuming a weak field dependence on the mobility. To calculate an average value of  $\mu$  which can be compared between films,  $\epsilon$  is taken to be approximately 3 and is assumed to not vary significantly with ferrocene,<sup>[73,4]</sup> and  $d$  is the layer thickness (200 nm). Using this method, we report an improvement in mobility increasing from  $2.12 \pm 0.05 \times 10^{-4} \text{ cm}^2 \text{ V}^{-1} \text{ s}^{-1}$  in the control up to  $3.59 \pm 0.05 \times 10^{-4} \text{ cm}^2 \text{ V}^{-1} \text{ s}^{-1}$  for the devices prepared with ferrocene shown in Figure 5c. The values are consistent with doped spiro-OMeTAD mobilities reported in the literature.<sup>[73,4,74]</sup> Comparing the ohmic region of the SCLC  $J$ - $V$  curves, we also observe an increase in conductivity in the spiro-OMeTAD films fabricated on a ferrocene layer. It is evident from these measurements the excess ferrocene diffusion into the spiro-OMeTAD can improve the charge carrier transport properties of the HTL. To demonstrate the positive effect of ferrocene on the spiro-OMeTAD, an additional set of archetypal  $\text{MAPbI}_3$  PSCs were prepared without using typical dopants (Figures S14–S15, Supporting Information). As expected, the undoped devices prepared using ferrocene exhibited significantly lower resistivity, improving the PCE from 3.98% in the control to up to 7.83% in the ferrocene modified devices.

$$J(V) = \left(\frac{9}{8}\right) \epsilon \epsilon_0 \mu \frac{V^2}{d^3} \quad (1)$$

To gain insight as to the potential mechanism behind the improvements to the carrier transport properties, UV-visible absorbance spectroscopy was conducted on Spiro-OMeTAD films prepared to match those used in the SCLC measurement (Figure 5d). To directly investigate the doping ability of ferrocene on the system, a third film was also prepared in which  $10 \text{ mg mL}^{-1}$  of ferrocene was directly added to the spiro-OMeTAD solution. Normalizing the absorbance peaks corresponding to neutral spiro-OMeTAD (385 nm) to that of the oxidized spiro-OMeTAD<sup>+</sup> (500 nm), we find that in both cases films prepared with ferrocene increase the concentration of oxidized spiro-OMeTAD<sup>+</sup> relative to the control.<sup>[72,75]</sup> We conclude that the observed mobility enhancement is from enhanced oxidation of the spiro-OMeTAD film occurring from ferrocene. Due to the redox potentials of the ferrocene and spiro-OMeTAD, this oxidation most likely occurs indirectly via the formation of superoxide radicals as has previously been demonstrated to oxidize spiro-OMeTAD.<sup>[76,77]</sup>

#### 2.4. Stability of Ferrocene Modified PSCs

Finally, we investigate the effect of ferrocene inclusion on PSC stability. In previous sections, it was demonstrated that ferrocene could form adducts with mobile  $\text{Li}^+$  ions rendering

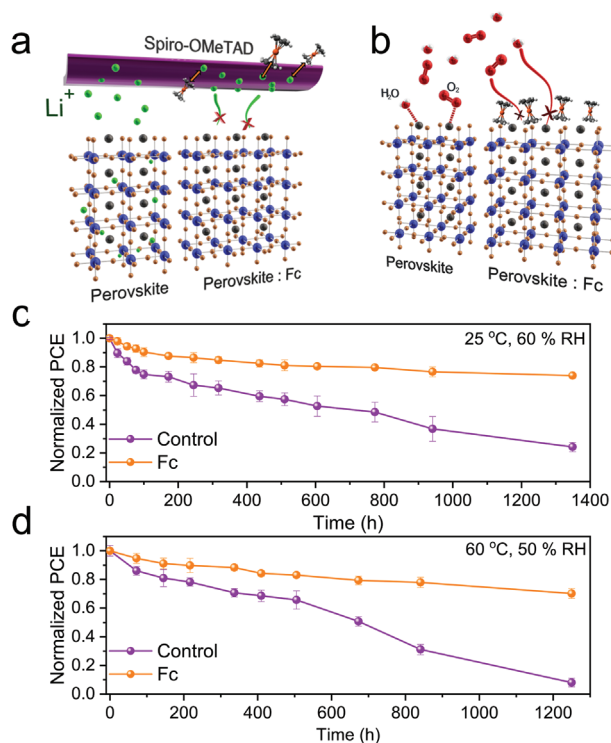


**Figure 6.** a) Schematic of  $\text{Li}^+$  immobilization via interaction with the cyclopentadiene rings of ferrocene leading to reduced migration of the  $\text{Li}^+$  through the PSC structure. b) Schematic of reduced interaction between oxygen and moisture in ferrocene modified perovskite surfaces. c) Normalized PCE of PSCs prepared with and without ferrocene, stored at 25 °C, RH = 60%. d) Accelerated stability study, PSCs prepared with and without ferrocene stored at 60 °C, RH = 50%.

them immobile, preventing migration within the perovskite and accumulation at the perovskite/spiro-OMeTAD interface (Figure 6a). In addition to the action of the electron-rich metalocene cyclopentadiene rings on the lithium cations, XPS also identified a reduction in the peak intensity at 288.5 eV in the perovskite films prepared with a ferrocene layer on the surface, relative to the C-C peak at 284.9 eV attributed to the ferrocene-modified perovskite surface (Figure S16, Supporting Information). The peak at 288.5 eV has previously been attributed to oxygen and moisture interacting with the perovskite surface and is an indicator of degradation occurring at the perovskite surface (Figure 6b).<sup>[78]</sup> The reduction of the interaction between the ferrocene-modified perovskite surface with oxygen and moisture affords greater tolerance to ambient conditions in ferrocene-containing PSCs.

To investigate the impact of the reduced lithium mobility and the ferrocene moisture blocking layer on stability, the performance of unencapsulated PSCs in a high relative humidity (25 °C, 60% RH) environment was tracked over an extended period of over 1350 hours. The data shows the devices prepared with ferrocene exhibit a significantly improved tolerance to the high humidity, retaining 74% of the initial PCE, as compared to 24% in the control devices as seen in Figure 6c. To accelerate degradation and investigate thermal stability, unencapsulated PSCs were also aged following ISOS-T-1 conditions,<sup>[79]</sup> (60 °C,

50% RH) over a period of 1250 hours shown in Figure 6d. It has previously been demonstrated that increasing the temperature increases the mobility of the  $\text{Li}^+$  ions within the device, significantly accelerating the degradation of PSCs.<sup>[7]</sup> Closely matching the high humidity measurement conducted at room temperature, we observe that ferrocene modified devices stored at elevated temperatures, exhibit outstanding improvements to the thermal stability, retaining 70% of the initial PCE, compared to 8% in PSCs prepared without ferrocene, over the 1250 hour storage period.<sup>[79]</sup> Poor intrinsic thermal stability at temperatures as low as 60 °C is a key challenge in using spiro-OMeTAD owing to the breaking down of the morphology,<sup>[80]</sup> fast tBP evaporation prompting LiTFSI to aggregate,<sup>[8]</sup> and increased mobile Li diffusion.<sup>[7]</sup> The reported data here demonstrates that thermal instability can be improved using ferrocene to anchor the lithium in place, preventing it from moving freely within operational PSCs.

Comparing the long-term stability of the PSCs both at elevated temperature and humidity, we identify a drop in PCE occurs in the PSCs prepared without ferrocene compared to those with ferrocene, starting at  $\approx 200$  h. This timeline is consistent with the timeline suggested by Wang et al. for LiTFSI mediated degradation of PSCs (200–1000 h) and coincides with the evaporation of tBP.<sup>[8]</sup> The improvements to the long-term stability of the PSCs further demonstrates that preventing the  $\text{Li}^+$  ions from becoming mobile within the PSC is essential and is consistent with our previous OrbiSIMS data showing reduced  $\text{Li}^+$  migration in films prepared with ferrocene (see Figures 1f,g). The data also shows films prepared with tBP exhibit significant  $\text{Li}^+$  migration and new methods to immobilize  $\text{Li}^+$  such as the use of ferrocene are required. Indeed, we report only a  $\sim 14\%$  drop in initial PCE between 200 and 1350 hours of storage at 60% RH, significantly less than the  $\approx 50\%$  decrease in initial PCE recorded in PSCs prepared without ferrocene as per Figure 6c.

The evaporation of tBP contributes significantly to the poor long-term stability of the spiro-OMeTAD as previously discussed by Wang et al.<sup>[8]</sup> To ensure ferrocene remained stable within the PSC even at high temperature, further stability measurements were collected at 85 °C and 100 °C (the sublimation temperature of ferrocene)(Figure S17, Supporting Information).<sup>[81]</sup> From the high-temperature stability measurements, we find that ferrocene does not show additional instability at high temperatures and can be assumed to remain stable within the PSC. Rather, the stability data reveals improved high-temperature tolerance in PSCs prepared with ferrocene.

Finally, the dark storage stability was evaluated following the ISOS D-1 stability test conditions (no illumination, 20% RH).<sup>[79]</sup> From this data we observed improved stability in devices prepared with ferrocene retaining 95% after 1100 hours, 10% higher than the control cell (Figure S18, Supporting Information). In this experiment the environmental moisture has been significantly lowered, reducing the destructive impact of hygroscopic LiTFSI and LiX salts within the PSC leading to significantly slower degradation. Comparing the dark storage data with the stability data collected at high humidity and elevated temperatures, the key destructive role of moisture and temperature on the degradation of conventional spiro-OMeTAD-based

devices is clear. From this data, the need for new approaches to target the dopant induced instability cannot be understated. Making the same comparison on the ferrocene prepared PSCs, a significantly reduced offset in stability is observed between the low humidity and high humidity stability data, further showing the key issues of spiro-OMeTAD stability have been addressed via the capturing of mobile Li<sup>+</sup> ions.

### 3. Conclusion

In conclusion, we have highlighted the impact of Li<sup>+</sup> ion migration from spiro-OMeTAD dopants on the long-term stability of high-efficiency PSCs. To tackle this, we demonstrate that the addition of ferrocene at the perovskite/spiro-OMeTAD interface is a highly effective strategy for coordinating the hygroscopic Li<sup>+</sup> ions, and rendering them immobile. From the OrbiSIMS depth profiling, we confirm that following the addition of the ferrocene layer, Li<sup>+</sup> ions do not migrate within the perovskite and aggregation at the interface is significantly reduced. Consequently, stability measurements conducted on the ferrocene-modified PSCs show significant improvements to the long-term stability across a range of conditions.

It is important that strategies to mitigate dopant-induced instability do not compromise device efficiency. To this end, we demonstrate that the addition of ferrocene does not reduce the facility when compared to a control cell with conventionally doped spiro-OMeTAD. Rather, by using a range of spectroscopies, we identify significantly improved hole extraction from the perovskite films into the spiro-OMeTAD attributed to the presence of interactions occurring between the ferrocene and Pb<sup>2+</sup> cations, at the perovskite surface. This higher yield of hole transfer in devices prepared using ferrocene shows promise for highly sensitive photodetectors. In addition, we also identify the ability of ferrocene to act like an organic dopant, enhancing the oxidation of spiro-OMeTAD. The observation that organometallobenes can improve the doping in organic semiconductors and has significant implications in the wider optoelectronic fields and merits further investigation.

Finally, we note the range of opportunities to further optimize the use of various organometallobenes as a strategy to tackle the intrinsic drawbacks to spiro-OMeTAD as an HTL. This can be achieved via exploiting the aromatic nature of the cyclopentadiene rings, opening the door to further designed structural functionalization, enabling further gains in device performance. Furthermore, while no 2D passivation has been used in this work to highlight the effect of the ferrocene, we expect the strategy demonstrated here to further enhance the highest efficiency devices within the literature, enabling record PSCs with appreciable efficiencies. Crucially, the insights offered here will enable leading high-efficiency devices to improve the stability, enabling a more balanced all-round technology. Indeed, it can be expected that with further optimization of both the device architecture and ferrocene functionality, the use of ferrocene at the perovskite/HTL interface can play a significant role in producing ever more efficient and crucially stable, spiro-OMeTAD-based devices.

### 4. Experimental Section

**Materials:** Lead iodide (PbI<sub>2</sub>) and lead bromide (PbBr<sub>2</sub>) were purchased from Tokyo Chemical Industry Co., Ltd (TCI). Formamidinium iodide (FAI) and methylammonium bromide (MABr) were purchased from GreatCell Solar. Methylammonium chloride (MACl), Lithium Bis(trifluoromethanesulfonyl)imide salt (LiTFSI) and 4-tert-butylpyridine (tBP) were obtained from Sigma-Aldrich. 2,2'',7,7''-Tetrakis(N,N-di-p-methoxyphenylamino)-9,9'-spirobifluorene (Spiro-OMeTAD, LT-S922), tris(2-(1*H*-pyrazol-1-yl)-4-tert-butylpyridine)-cobalt(III)tris(bis(trifluoromethylsulfonyl)imide) (FK209) were purchased from Xi'an Polymer Light Technology. Ferrocene powder was purchased from Tanyuchem chemicals. *N,N*-dimethylformamide (DMF), dimethyl sulfoxide (DMSO), chlorobenzene (CB), acetonitrile (ACN) and ethyl acetate (EA) were purchased from Sigma-Aldrich and without further purification.

**Device Fabrication:** The etched fluorine-doped SnO<sub>2</sub> (FTO) substrates were treated by ultraviolet-ozone cleaner for 15 min. Then the SnO<sub>2</sub> layer was fabricated by the chemical bath deposition method described in previous literature.<sup>[1]</sup> The perovskite films were fabricated from a precursor solution of mixing 1.4 M FAPbI<sub>3</sub> and 5 mol% MAPbBr<sub>3</sub> in DMF:DMSO = 8:1 with excess PbI<sub>2</sub> (9 mol%) and 0.5 M MACl. The precursor solution was spin-coated at 1000 r.p.m. for 10 s and at 5000 r.p.m. for 30 s. At the time of 20 s of the whole process, 120 μL of ethyl acetate was dripped on the spinning substrate, followed by annealing at 100 °C for 60 min. After the substrate cooling down, the perovskite film was spin-coated with 5 mg mL<sup>-1</sup> – 15 mg mL<sup>-1</sup> ferrocene solution (dissolved in CB) at 4000 r.p.m. for 30 s. Subsequently, the spiro-OMeTAD in chlorobenzene (90 mg mL<sup>-1</sup>) solution with the addition of 39 μL tBP, 23 μL Li-TFSI (520 mg mL<sup>-1</sup> in acetonitrile) and 10 μL FK209 (300 mg mL<sup>-1</sup> in acetonitrile) was deposited on the perovskite film dynamically at 4000 r.p.m. for 20 s. Finally, a 100 nm Au electrode was deposited by thermal evaporation. SCLC devices were prepared by conducting UV ozone treatment on ITO substrates. The ITO substrates were washed with chlorobenzene to improve wetting. Ferrocene and spiro-OMeTAD were deposited using the methods previously mentioned. Spiro-OMeTAD was spin-coated at 2000 rpm for SCLC devices.

**Surface Microscopy:** The surface morphologies were measured by a field emission SEM (Jeol 7100F). Atom force microscopy (AFM) was carried out using Bruker Multimode 8 scanning probe microscope (tapping and phase-amplitude modes). Kelvin probe force microscopy (KPFM) was conducted using an Antimony (n) doped Si tip. A HOPG sample was measured as a reference surface and is presented in the SI (Figure S19, Supporting Information). Energy dispersive X-ray (EDX) spectroscopy was conducted using an x-act Oxford Instrument system.

**X-ray Diffraction:** The crystallographic XRD data for the samples in this work were collected using a PANalytical X'Pert Pro powder diffractometer in a Bragg-Brentano geometry (step size 0.004°) using a Cu Kα target (45 kV). For Grazing incidence X-ray diffraction (GIXRD), the incident angle between the X-ray source and sample was set to 0.2°.

**<sup>7</sup>Li and <sup>13</sup>C NMR:** Samples for NMR were dissolved in CDCl<sub>3</sub> and measured on a Bruker Avance III HD 400 NMR, collected with topspin 3.2 software.

**PL and TRPL:** Steady-state and time-resolved PL were measured using Edinburgh Instrument FLS1000 by exciting the samples at 375 nm. A Xenon lamp was used for steady-state PL and a picosecond laser was used for time-resolved measurements.

**J-V Measurements:** The current-voltage characteristics of perovskite solar cells were carried out in air using a Keysight B2901A source meter under standard AM 1.5 G illumination (100 mW cm<sup>-2</sup>) with a solar simulator (Enli Technology Co. Ltd., Taiwan, SS-F5-3A). The light intensity was calibrated by a standard monocrystalline silicon solar cell with a KG-5 filter. Both reverse scan (from 1.2 to -0.2 V, step 0.02 V) and forward scan (from -0.2 to 1.2 V, step 0.02 V) was carried out with a delay time of 100 ms. The stabilized power output was carried out by setting the bias voltage to the initial V<sub>MPP</sub> which was determined from the J-V curve. The active area was determined by a 0.09 cm<sup>2</sup> metal mask. External quantum efficiency (EQE) spectra were measured using Bentham PVE 300 system. SCLC was conducted on hole-only devices using spiro-OMeTAD with thickness 200 nm using a B2901A source meter.

**Transient Photovoltage/Photocurrent:** Transient photovoltage and photocurrent (TPV/TPC) were measured using a white light LED source at suns illumination to bias the device. The distance of the bulb was adjusted to yield a photovoltage in the PSC equivalent to the  $V_{OC}$ . A green LED was used to create a perturbation in carriers via pulsing for 5  $\mu$ s at 30 kHz using an Agilent 8114A pulse generator. The photocurrent decay following a perturbation at open circuit condition was measured across a 1 M $\Omega$  input impedance using a Tektronix MDO3014 1 GHz digital oscilloscope.

**X-ray Photoelectron Spectroscopy:** X-ray photoelectron spectroscopy (XPS) was carried out on a Thermo Fisher Scientific K-Alpha instrument, using Al K $\alpha$  radiation (1486.6 eV). Survey spectra were taken at a pass energy of 200 eV. High resolution C 1s, Fe 2p, Pb 4f and Li 1s were taken at a pass energy of 50 eV. Charge neutralisation was carried out using a dual-beam Ar<sup>+</sup> and electron flood gun. Charge correction of spectra was carried out using adventitious C 1s set to a binding energy of 285.0 eV.

**Electrical Impedance Spectroscopy:** The electrical impedance spectra were recorded on the all-in-one Paios characterization platform by Fluxim AG (www.fluxim.com/paios). The oscillating voltage signal was set to 70 mV.

**Transient Absorption Spectroscopy:** Transient absorption spectroscopy (TAS): Samples were prepared using an electron extracting mesoporous titanium oxide (mp-TiO<sub>2</sub>) substrate to ensure efficient extraction of electrons from the perovskite. An mp-TiO<sub>2</sub> film was prepared via spin-coating a solution of mp-TiO<sub>2</sub> (TiO<sub>2</sub>:EtOH = 2:7) and spin coating at 6000 r.p.m. Perovskite, ferrocene and spiro-OMeTAD films were sequentially deposited using the previously described methods.

Samples for microsecond transient absorption spectroscopy measurements were stored in a nitrogen-filled glovebox and taken in a sealed quartz cuvette for measurement. Excitation was achieved with a dye laser, which was itself pumped by an N<sub>2</sub> laser (Photon Technology International Inc. GL-3300). The laser fluence at the point of measurement was 15  $\mu$ J cm<sup>-2</sup>. The transient changes in the absorption of the sample were captured with a 100 W tungsten lamp (Bentham IL 1) on an orthogonal optical axis to the excitation beam. The probe wavelength was adjusted by a monochromator and set to 1600 nm – the maximum of the transient spectrum of the spiro-OMeTAD hole polaron. This probing beam was detected by an InGaAs photodiode (Hamatsu Photonics) before being filtered and amplified (Costronics Electronics) and finally interpreted by a digital oscilloscope (Tektronics DPO3012). TAS decays were modelled with a stretched exponential

function:  $\Delta OD \propto \exp\left[-\left(\frac{t}{\tau_0}\right)^a\right]$ . Given the complex decay dynamics, an approximate lifetime,  $\tau_{rec}$  is assigned as the time taken for  $\Delta OD$  to reach 50% of its original value.

**Time of Flight Secondary Ion Mass Spectrometry (ToF-SIMS):** ToF-SIMS 3D mapping of spiro-OMeTAD films with and without ferrocene was carried out using a high-resolution 3D OrbiSIMS (HybridSIMS) instrument from IONTOF GmbH.<sup>[52]</sup> ToF-SIMS data were acquired in positive ion polarity mode in dual-beam mode by raster scanning a 30 keV Bi<sub>3</sub><sup>+</sup> primary ion beam (delivering 0.1 pA) of 100  $\times$  100  $\mu$ m<sup>2</sup> at the center of a 400  $\times$  400  $\mu$ m<sup>2</sup> sputter crater formed using an argon GCIB. The GCIB was operated with 10 keV and 1460 atoms in the cluster with a 3 nA beam current. The analysis was performed in the “non-interlaced” mode with a low-energy (20 eV) electron flood gun employed to neutralize charge build-up. For the setting, three shots/pixel/frame were used per cycle with 1 analysis scan per cycle and a pause time in between cycles of 1 s. The ToF analyzer was set with a 200  $\mu$ s cycle time, resulting in a mass range between 0 and 2233 mass units. 80 scans were conducted with a total sputter time of 115 seconds. Internal mass calibration was carried out by using Li<sup>+</sup>, Na<sup>+</sup>, C<sub>2</sub>H<sub>3</sub><sup>+</sup>, C<sub>3</sub>H<sub>5</sub><sup>+</sup> and C<sub>5</sub>H<sub>9</sub><sup>+</sup> mass signals in positive ion mode. Data analysis of the ToF-SIMS measurements was done with Surface Lab software version 7.1 (IONTOF GmbH, Muenster, Germany).

## Supporting Information

Supporting Information is available from the Wiley Online Library or from the author.

## Acknowledgements

T.W. gratefully acknowledges the help of Dr. Driscoll with X-ray diffraction training and maintenance. T.W. also thanks Leanne Baker for the chemical structural drawings.

**Funding Sources:** T.W. gratefully thanks the University of Surrey doctoral college for their support through the DCSA3 scheme. X.L. acknowledges the stipend support from Zhengzhou University and University of Surrey studentship. S.J. received funding from the European Union's Horizon 2020 Research and Innovation Program under Grant Agreement No. 953187 (MUSICODE). K.D.G.I.J. gratefully acknowledges financial support from the Equality Foundation of Hong Kong. W.H.K.P. acknowledges support from the University of Surrey Doctoral College Studentship scheme. S.K., D.S., and M.A. acknowledge the financial support of this work by the Engineering and Physical Sciences Research Council (EPSRC) grant “3D OrbiSIMS: Label free chemical imaging of materials, cells and tissue” (Grant Code EP/P029868/1). T.J.M. thanks the Royal Commission for the Exhibition of 1851 for their financial support through a Research Fellowship. S.A.H. acknowledges financial support from EPSRC (Grant Number EP/R020574/1) and the UKRI Global Challenge Research Fund project SUNRISE (Grant Number EP/P032591/1). S.J.S. gratefully acknowledges the support of EPSRC (UK) under Grant Number EP/N021037/1. W.Z. acknowledges UK Engineering and Physical Sciences Research Council (EPSRC) New Investigator Award (2018; EP/R043272/1) and Newton Advanced Fellowship (192097) for financial support.

## Conflict of Interest

The authors declare no conflict of interest.

## Author Contributions

T.W. and X.L. contributed equally to this work. T.W. conceived the idea of the work. T.W. designed the project and directed experiments. T.W. plotted data and drafted the manuscript. X.L. and T.W. prepared samples. X.L. prepared high-efficiency devices with doped spiro-OMeTAD. T.W. prepared undoped devices. R.J.W. conducted TAS measurements, plotted and analyzed data, supervised by S.A.H. S.K., D.S. and M.A. conducted ToF-SIMS measurements. M.T.S. Conducted PL and TRPL measurements. S.J. conducted EIS and capacitance measurements. T.J.M. and S.S. conducted XPS measurements. T.W. and I.M. conducted TPV and TPC, supervised by S.J.S. T.W. conducted XRD, GIXRD, AFM, KPFM, EDX, SCLC. T.W. conducted NMR, supervised by S.A.H. X.L. conducted device characterization, EQE, stability measurements and SEM. S.J.S., K.D.G.I.J. helped coordinate the project, contributed to the analysis of electrical characterization. W.Z., S.A.H. and S.J.S. supervised the research. All authors contributed to the discussion of the results and writing of the manuscript.

## Data Availability Statement

The data that support the findings of this study are available from the corresponding author upon reasonable request.

## Keywords

ferrocene, heterojunction engineering, LiTFSI, perovskites, spiro-OMeTAD

Received: February 25, 2022

Revised: April 7, 2022

Published online:

- [1] J. J. Yoo, G. Seo, M. R. Chua, T. G. Park, Y. Lu, F. Rotermund, Y.-K. Kim, C. S. Moon, N. J. Jeon, J.-P. Correa-Baena, V. Bulović, S. S. Shin, M. G. Bawendi, J. Seo, *Nature* **2021**, 590, 587.
- [2] J. Jeong, M. Kim, J. Seo, H. Lu, P. Ahlawat, A. Mishra, Y. Yang, M. A. Hope, F. T. Eickemeyer, M. Kim, Y. J. Yoon, I. W. Choi, B. P. Darwich, S. J. Choi, Y. Jo, J. H. Lee, B. Walker, S. M. Zakeeruddin, L. Emsley, U. Rothlisberger, A. Hagfeldt, D. S. Kim, M. Grätzel, J. Y. Kim, *Nature* **2021**, 592, 381.
- [3] H. Min, D. Y. Lee, J. Kim, G. Kim, K. S. Lee, J. Kim, M. J. Paik, Y. K. Kim, K. S. Kim, M. G. Kim, T. J. Shin, S. Il Seok, *Nature* **2021**, 598, 444.
- [4] H. J. Snaith, M. Grätzel, *Appl. Phys. Lett.* **2006**, 89, 262114.
- [5] F. M. Rombach, S. A. Haque, T. J. Macdonald, *Energy Environ. Sci.* **2021**, 10.1039/D1EE02095A.
- [6] G. Ren, W. Han, Y. Deng, W. Wu, Z. Li, J. Guo, H. Bao, C. Liu, W. Guo, *J. Mater. Chem. A* **2021**, 9, 4589.
- [7] S.-G. Kim, T. H. Le, T. de Monfreid, F. Goubard, T.-T. Bui, N.-G. Park, *Adv. Mater.* **2021**, 33, 2007431.
- [8] S. Wang, M. Sina, P. Parikh, T. Uekert, B. Shahbazian, A. Devaraj, Y. S. Meng, *Nano Lett.* **2016**, 16, 5594.
- [9] C. Ding, R. Huang, C. Ahläng, J. Lin, L. Zhang, D. Zhang, Q. Luo, F. Li, R. Österbacka, C.-Q. Ma, *J. Mater. Chem. A* **2021**, 9, 7575.
- [10] C. Xiao, F. Zhang, Z. Li, S. P. Harvey, X. Chen, K. Wang, C.-S. Jiang, K. Zhu, M. Al-Jassim, *Matter* **2020**, 2, 261.
- [11] X. Guo, J. Li, B. Wang, P. Zeng, F. Li, Q. Yang, Y. Chen, M. Liu, *ACS Appl. Energy Mater.* **2020**, 3, 970.
- [12] Y. Zhang, A. Kirs, F. Ambroz, C.-T. Lin, A. S. R. Bati, I. P. Parkin, J. G. Shapter, M. Batmunkh, T. J. Macdonald, *Small Methods* **2021**, 5, 2000744.
- [13] J. A. Dawson, A. J. Naylor, C. Eames, M. Roberts, W. Zhang, H. J. Snaith, P. G. Bruce, M. S. Islam, *ACS Energy Lett.* **2017**, 2, 1818.
- [14] Z. Li, C. Xiao, Y. Yang, S. P. Harvey, D. H. Kim, J. A. Christians, M. Yang, P. Schulz, S. U. Nanayakkara, C.-S. Jiang, J. M. Luther, J. J. Berry, M. C. Beard, M. M. Al-Jassim, K. Zhu, *Energy Environ. Sci.* **2017**, 10, 1234.
- [15] Q. Jiang, Y. Zhao, X. Zhang, X. Yang, Y. Chen, Z. Chu, Q. Ye, X. Li, Z. Yin, J. You, *Nat. Photonics* **2019**, 13, 460.
- [16] C. Li, J. Wei, M. Sato, H. Koike, Z.-Z. Xie, Y.-Q. Li, K. Kanai, S. Kera, N. Ueno, J.-X. Tang, *ACS Appl. Mater. Interfaces* **2016**, 8, 11526.
- [17] B. Tan, S. R. Raga, K. J. Rietwyk, J. Lu, S. O. Furer, J. C. Griffith, Y.-B. Cheng, U. Bach, *Nano Energy* **2021**, 82, 105658.
- [18] Y. Yang, M. T. Hoang, D. Yao, N. D. Pham, V. T. Tiong, X. Wang, H. Wang, *J. Mater. Chem. A* **2020**, 8, 12723.
- [19] L.-L. Jiang, Z.-K. Wang, M. Li, C.-H. Li, P.-F. Fang, L.-S. Liao, *J. Mater. Chem. A* **2019**, 7, 3655.
- [20] J.-Y. Seo, S. Akin, M. Zalibera, M. A. R. Preciado, H.-S. Kim, S. M. Zakeeruddin, J. V. Milić, M. Grätzel, *Adv. Funct. Mater.* **2021**, 31, 2102124.
- [21] J.-Y. Seo, H.-S. Kim, S. Akin, M. Stojanovic, E. Simon, M. Fleischer, A. Hagfeldt, S. M. Zakeeruddin, M. Grätzel, *Energy Environ. Sci.* **2018**, 11, 2985.
- [22] N. D. Pham, J. Shang, Y. Yang, M. T. Hoang, V. T. Tiong, X. Wang, L. Fan, P. Chen, L. Kou, L. Wang, H. Wang, *Nano Energy* **2020**, 69, 104412.
- [23] M. Li, Z.-K. Wang, Y.-G. Yang, Y. Hu, S.-L. Feng, J.-M. Wang, X.-Y. Gao, L.-S. Liao, *Adv. Energy Mater.* **2016**, 6, 1601156.
- [24] G. Zhu, L. Yang, C. Zhang, G. Du, N. Fan, Z. Luo, X. Zhang, J. Zhang, *ACS Appl. Energy Mater.* **2022**, 5, 3595.
- [25] M. Jeong, I. W. Choi, E. M. Go, Y. Cho, M. Kim, B. Lee, S. Jeong, Y. Jo, H. W. Choi, J. Lee, J.-H. Bae, S. K. Kwak, D. S. Kim, C. Yang, *Science* **2020**, 369, 1615.
- [26] B. Park, B. Philippe, S. M. Jain, X. Zhang, T. Edvinsson, H. Rensmo, B. Zietz, G. Boschloo, *J. Mater. Chem. A* **2015**, 3, 21760.
- [27] J.-W. Lee, D.-H. Kim, H.-S. Kim, S.-W. Seo, S. M. Cho, N.-G. Park, *Adv. Energy Mater.* **2015**, 5, 1501310.
- [28] M. Saliba, T. Matsui, J.-Y. Seo, K. Domanski, J.-P. Correa-Baena, M. K. Nazeeruddin, S. M. Zakeeruddin, W. Tress, A. Abate, A. Hagfeldt, M. Grätzel, *Energy Environ. Sci.* **2016**, 9, 1989.
- [29] H. Zai, C. Zhu, H. Xie, Y. Zhao, C. Shi, Z. Chen, X. Ke, M. Sui, C. Chen, J. Hu, Q. Zhang, Y. Gao, H. Zhou, Y. Li, Q. Chen, *ACS Energy Lett.* **2018**, 3, 30.
- [30] A. Fakharuddin, L. Schmidt-Mende, G. Garcia-Belmonte, R. Jose, I. Mora-Sero, *Adv. Energy Mater.* **2017**, 7, 1700623.
- [31] S. Shao, M. A. Loi, *Adv. Mater. Interfaces* **2020**, 7, 1901469.
- [32] Z. Ni, C. Bao, Y. Liu, Q. Jiang, W.-Q. Wu, S. Chen, X. Dai, B. Chen, B. Hartweg, Z. Yu, Z. Holman, J. Huang, *Science* **2020**, 367, 1352 LP.
- [33] S. Shao, J. Liu, H.-H. Fang, L. Qiu, G. H. ten Brink, J. C. Hummelen, L. J. A. Koster, M. A. Loi, *Adv. Energy Mater.* **2017**, 7, 1701305.
- [34] R. J. E. Westbrook, T. J. Macdonald, W. Xu, L. Lanzetta, J. M. Marin-Beloqui, T. M. Clarke, S. A. Haque, *J. Am. Chem. Soc.* **2021**, 143, 12230.
- [35] T. Zhang, M. Long, M. Qin, X. Lu, S. Chen, F. Xie, L. Gong, J. Chen, M. Chu, Q. Miao, Z. Chen, W. Xu, P. Liu, W. Xie, J. Xu, *Joule* **2018**, 2, 2706.
- [36] T. Webb, S. J. Sweeney, W. Zhang, *Adv. Funct. Mater.* **2021**, 2103121.
- [37] M. A. Mahmud, T. Duong, J. Peng, Y. Wu, H. Shen, D. Walter, H. T. Nguyen, N. Mozaffari, G. D. Tabi, K. R. Catchpole, K. J. Weber, T. P. White, *Adv. Funct. Mater.* n.d., n/a, 2009164.
- [38] R. J. E. Westbrook, W. Xu, X. Liang, T. Webb, T. M. Clarke, S. A. Haque, *J. Phys. Chem. Lett.* **2021**, 12, 3312.
- [39] X. Liu, T. Webb, L. Dai, K. Ji, J. A. Smith, R. C. Kilbride, M. Yavari, J. Bi, A. Ren, Y. Huang, Z. Wang, Y. Shen, G. Shao, S. J. Sweeney, S. Hinder, H. Li, D. G. Lidzey, S. D. Stranks, N. C. Greenham, S. R. P. Silva, W. Zhang, *Energy Environ. Mater.* **2021**. <https://doi.org/10.1002/eem2.12321>
- [40] T. W. Hamann, O. K. Farha, J. T. Hupp, *J. Phys. Chem. C* **2008**, 112, 19756.
- [41] S. Sönmezoglu, C. Akyürek, S. Akin, *J. Phys. D: Appl. Phys.* **2012**, 45, 425101.
- [42] T. Daeneke, A. J. Mozer, T.-H. Kwon, N. W. Duffy, A. B. Holmes, U. Bach, L. Spiccia, *Energy Environ. Sci.* **2012**, 5, 7090.
- [43] Y. Saygili, M. Stojanovic, N. Flores-Díaz, S. M. Zakeeruddin, N. Vlachopoulos, M. Grätzel, A. Hagfeldt, *Inorganics* **2019**, 7, 30.
- [44] S. Cazzanti, C. Caramori, R. Argazzi, C. M. Elliott, C. A. Bignozzi, *J. Am. Chem. Soc.* **2006**, 128, 9996.
- [45] A. Ghosh, S. Mishra, S. Giri, S. M. Mobin, A. Bera, S. Chatterjee, *Organometallics* **2018**, 37, 1999.
- [46] G. Kalita, S. Sharma, K. Wakita, M. Umeno, Y. Hayashi, M. Tanemura, *Phys. Chem. Chem. Phys.* **2013**, 15, 1271.
- [47] C. Oelsner, M. A. Herrero, C. Ehli, M. Prato, D. M. Guldi, *J. Am. Chem. Soc.* **2011**, 133, 18696.
- [48] S. Vanicek, M. Podewitz, J. Stubbe, D. Schulze, H. Kopacka, K. Wurst, T. Müller, P. Lippmann, S. Haslinger, H. Schottenberger, K. R. Liedl, I. Ott, B. Sarkar, B. Bildstein, *Chem. Eur. Journal* **2018**, 24, 3742.
- [49] A. Hildebrandt, H. Lang, *Organometallics* **2013**, 32, 5640.
- [50] L. Ye, Y. Cai, C. Li, L. Zhu, J. Xu, K. Weng, K. Zhang, M. Huang, M. Zeng, T. Li, E. Zhou, S. Tan, X. Hao, Y. Yi, F. Liu, Z. Wang, X. Zhan, Y. Sun, *Energy Environ. Sci.* **2020**, 13, 5117.
- [51] J. T. DuBose, P. V. Kamat, *J. Phys. Chem. Lett.* **2019**, 10, 6074.
- [52] M. K. Passarelli, A. Pirkl, R. Moellers, D. Grinfeld, F. Kollmer, R. Havelund, C. F. Newman, P. S. Marshall, H. Arlinghaus, M. R. Alexander, A. West, S. Horning, E. Niehuis, A. Makarov, C. T. Dollyer, I. S. Gilmore, *Nat. Methods* **2017**, 14, 1175.
- [53] A. Priebe, T. Xie, G. Bürki, L. Pethö, J. Michler, *J. Anal. At. Spectrom.* **2020**, 35, 1156.
- [54] A. H. Ilkhechi, J. M. Mercero, I. Silanes, M. Bolte, M. Scheibitz, H.-W. Lerner, J. M. Ugalde, M. Wagner, *J. Am. Chem. Soc.* **2005**, 127, 10656.

- [55] Z. Liu, L. Feng, X. Su, C. Qin, K. Zhao, F. Hu, M. Zhou, Y. Xia, *J. Power Sources* **2018**, 375, 102.
- [56] A. Le Goff, V. Artero, R. Metayé, F. Moggia, B. Jusselme, M. Razavet, P. D. Tran, S. Palacin, M. Fontecave, *Int. J. Hydrogen Energy* **2010**, 35, 10790.
- [57] G. Pilatos, A. V. Perdikaki, A. Sapalidis, G. S. Pappas, T. Giannakopoulou, D. Tsoutsou, E. Xenogiannopoulou, N. Boukos, A. Dimoulas, C. Trapalis, N. K. Kanellopoulos, G. N. Karanikolos, *J. Appl. Phys.* **2016**, 119, 064303.
- [58] B. Li, W. Wu, T. Zhang, S. Jiang, X. Chen, G. Zhang, X. Zhang, *RSC Adv.* **2017**, 7, 38691.
- [59] Q. Chang, F. Wang, W. Xu, A. Wang, Y. Liu, J. Wang, Y. Yun, S. Gao, K. Xiao, L. Zhang, L. Wang, J. Wang, W. Huang, T. Qin, *Angew. Chem., Int. Ed.* **2021**, 60, 25567.
- [60] S. A. L. Weber, I. M. Hermes, S.-H. Turren-Cruz, C. Gort, V. W. Bergmann, L. Gilson, A. Hagfeldt, M. Graetzel, W. Tress, R. Berger, *Energy Environ. Sci.* **2018**, 11, 2404.
- [61] H. Kanda, N. Shibayama, A. J. Huckaba, Y. Lee, S. Paek, N. Klipfel, C. Roldán-Carmona, V. I. E. Queloz, G. Grancini, Y. Zhang, M. Abuhelaiqa, K. T. Cho, M. Li, M. D. Mensi, S. Kinge, M. K. Nazeeruddin, *Energy Environ. Sci.* **2020**, 13, 1222.
- [62] A. Marchioro, J. Teuscher, D. Friedrich, M. Kunst, R. van de Krol, T. Moehl, M. Grätzel, J.-E. Moser, *Nature Photon* **2014**, 8, 250.
- [63] R. J. E. Westbrook, D. r. I. Sanchez-Molina, D. r. J. M. Marin-Beloqui, D. r. H. Bronstein, D. r. S. A. Haque, *J. Phys. Chem. C* **2018**, 122, 1326.
- [64] N. Guijarro, T. Lutz, T. Lana-Villarreal, F. O'Mahony, R. Gómez, S. A. Haque, *J. Phys. Chem. Lett.* **2012**, 3, 1351.
- [65] F. T. F. O'Mahony, Y. H. Lee, C. Jellott, S. Dmitrov, D. T. J. Bryant, J. R. Durrant, B. C. O'Regan, M. Graetzel, M. K. Nazeeruddin, S. A. Haque, *J. Mater. Chem. A* **2015**, 3, 7219.
- [66] F. T. F. O'Mahony, T. Lutz, N. Guijarro, R. Gómez, S. A. Haque, *Energy Environ. Sci.* **2012**, 5, 9760.
- [67] H. C. Leventis, F. O'Mahony, J. Akhtar, M. Afzaal, P. O'Brien, S. A. Haque, *J. Am. Chem. Soc.* **2010**, 132, 2743.
- [68] S. A. Haque, T. Park, A. B. Holmes, J. R. Durrant, *ChemPhysChem* **2003**, 4, 89.
- [69] M. M. Tavakoli, W. Tress, J. V. Milić, D. Kubicki, L. Emsley, M. Grätzel, *Energy Environ. Sci.* **2018**, 11, 3310.
- [70] R. Hidayat, A. A. Nurunnizar, A. Fariz, Herman, E. S. R. , Shobih, T. O. , A. Fujii, M. Ozaki, *Sci. Rep.* **2020**, 10, 19197.
- [71] S. Shao, M. Abdu-Aguye, L. Qiu, L.-H. Lai, J. Liu, S. Adjokatse, F. Jahani, M. E. Kamminga, G. H. ten Brink, T. T. M. Palstra, B. J. Kooi, J. C. Hummelen, M. A. Loi, *Energy Environ. Sci.* **2016**, 9, 2444.
- [72] W. H. Nguyen, C. D. Bailie, E. L. Unger, M. D. McGehee, *J. Am. Chem. Soc.* **2014**, 136, 10996.
- [73] D. Poplavskyy, J. Nelson, *J. Appl. Phys.* **2002**, 93, 341.
- [74] J.-Y. Seo, H.-S. Kim, S. Akin, M. Stojanovic, E. Simon, M. Fleischer, A. Hagfeldt, S. M. Zakeeruddin, M. Grätzel, *Energy Environ. Sci.* **2018**, 11, 2985.
- [75] R. Schöllin, M. H. Karlsson, S. K. Eriksson, H. Siegbahn, E. M. J. Johansson, H. Rensmo, *J. Phys. Chem. C* **2012**, 116, 26300.
- [76] S. Wang, W. Yuan, Y. S. Meng, *ACS Appl. Mater. Interfaces* **2015**, 7, 24791.
- [77] M. Hayyan, M. A. Hashim, I. M. AlNashef, *Chem. Rev.* **2016**, 116, 3029.
- [78] H. Zhu, Y. Liu, F. T. Eickemeyer, L. Pan, D. Ren, M. A. Ruiz-Preciado, B. Carlsen, B. Yang, X. Dong, Z. Wang, H. Liu, S. Wang, S. M. Zakeeruddin, A. Hagfeldt, M. I. Dar, X. Li, M. Grätzel, *Adv. Mater.* **2020**, 32, 1907757.
- [79] M. V. Khenkin, E. A. Katz, A. Abate, G. Bardizza, J. J. Berry, C. Brabec, F. Brunetti, V. Bulović, Q. Burlingame, A. Di Carlo, R. Cheacharoen, Y.-B. Cheng, A. Colmann, S. Cros, K. Domanski, M. Duszka, C. J. Fell, S. R. Forrest, Y. Galagan, D. Di Girolamo, M. Grätzel, A. Hagfeldt, E. von Hauff, H. Hoppe, J. Kettle, H. Köbler, M. S. Leite, S. (Frank) Liu, Y.-L. Loo, J. M. Luther, et al., *Nat. Energy* **2020**, 5, 35.
- [80] T. Malinauskas, D. Tomkute-Luksiene, R. Sens, M. Daskeviciene, R. Send, H. Wonneberger, V. Jankauskas, I. Bruder, V. Getautis, *ACS Appl. Mater. Interfaces* **2015**, 7, 11107.
- [81] J. W. Edwards, G. L. Kington, R. Mason, *Trans. Faraday Soc.* **1960**, 56, 660.